Supplementary Information

A radially confined point discharge microplasma for a miniaturized optical emission spectrometer

Wen Zeng,[a] Tao Lin,[ac] Qinsong Tang,[a] Xiaoming Jiang *[a] and Xiandeng Hou *[ab]

[a]Analytical & Testing Center, Sichuan University, Chengdu, Sichuan, 610064, China.
[b]Key Laboratory of Green Chemistry & Technology of MOE, College of Chemistry, Sichuan University, Chengdu, Sichuan 610064, China.
[c]Electric Power Research Institute of State Grid Anhui Electric Power Co., Ltd., Hefei, Anhui 230601, China.

* Corresponding authors' emails: houxd@scu.edu.cn; jiangxm@scu.edu.cn

Table of Contents

1. Reagents and samples

All chemical reagents used in this work were at least analytical grade. High-purity Ar (99.999%) was from Qiaoyuan Gas Co., Ltd. (Chengdu, China). Deionized water (DIW, 18.2 MΩ cm) was prepared with a water purification system (PCUJ-10, Chengdu Pincheng Technology Co., Ltd., Chengdu, China). KBH_4, KOH, HCl, thiourea, ascorbic acid, and $K_3[Fe(CN)_6]$ were purchased from Chengdu Chron Chemicals (Chengdu, China). The interferences ion solutions of Ca^{2+}, Na^{+}, Mg^{2+}, Al^{3+}, Zn^{2+}, Fe^{3+}, Co^{2+}, Ni^{2+}, and Cu^{2+} used in interference study were prepared by dissolving its chloride inorganic salts, all of which from the Chengdu Chron Chemicals (Chengdu, China). Certified Reference Materials (CRMs) of soil (GBW07405 and GBW07311) were bought from the National Research Center for Certified Reference Materials (NRCCRM, Beijing, China). The water sample (GBW(E)081536) was purchased from the National Institute of Metrology (Beijing, China). Standard samples of selenium-enriched yeast (SELM-1) and biological samples (lobster hepatopancreas, TORT-3; and dogfish liver, DOLT-5) were from the National Research Council Canada (NRC, Canada).

All the samples were processed by microwave-assisted digestion except for the water sample, and three replicates were prepared for each. After dried to a constant weight, the soil samples (GBW07405 and GBW07311), selenium-enriched yeast (SELM-1), and biological samples (TORT-3 and DOLT-5) were accurately weighed 0.2 g into Teflon digestion vessels, respectively, then 6 mL HNO_3 and 2 mL H_2O_2 were added to the samples, and additional 2 mL HF was added for soil samples. The sealed digestion tanks were placed into a microwave digestion system (Multiwave PRO, Anton Paar) and heated for digestion according to the following procedures: 15 min at 150 ºC, and 35 min at 180 ºC with a gradual decrease to 70 ºC. After digestion, the Teflon digestion vessels containing digested samples were transferred to the electric hot plate (EG20A, LabTech Co., Beijing, China) and evaporated to near dryness at 100 ºC. The residual solution was removed and diluted to 20 mL with 10% (v/v) HCl solution for subsequent analysis. The sample blanks were treated with the same procedure along with these samples.

2. Characteristic emission spectra

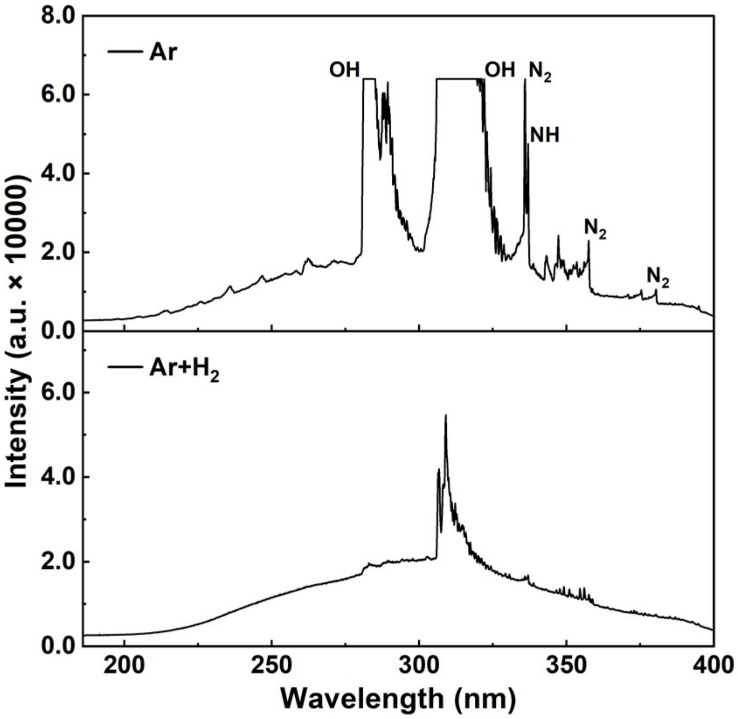

Fig. S1 Characteristic emission spectra of Ar and Ar+H_2. The molecular emission bands including OH (283, 309 nm), NH (337 nm), and N_2 (336, 358, 380 nm) presented in the background emission spectra of pure Ar plasma, which were significantly suppressed owing to the by-product hydrogen gas generated during the HG process.

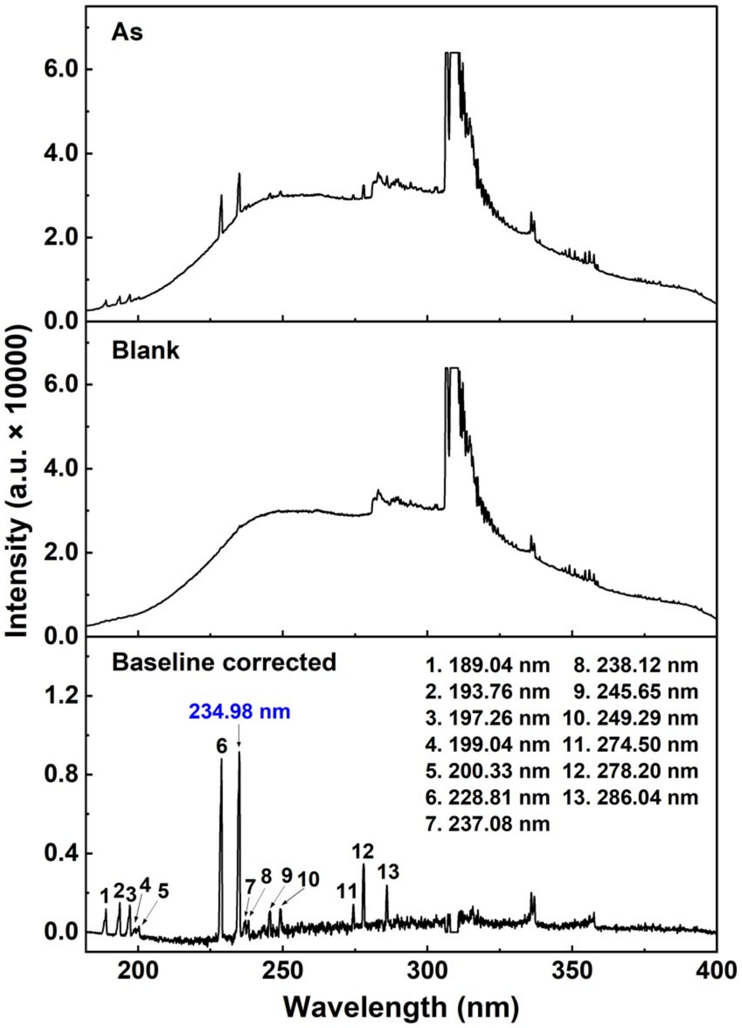

Fig. S2 Characteristic emission spectra of sample (As), blank (Ar+H_2), and the spectra after baseline corrected. Experimental details: 0.5 mg L^{-1} As; and CCD integration time, 100 ms.

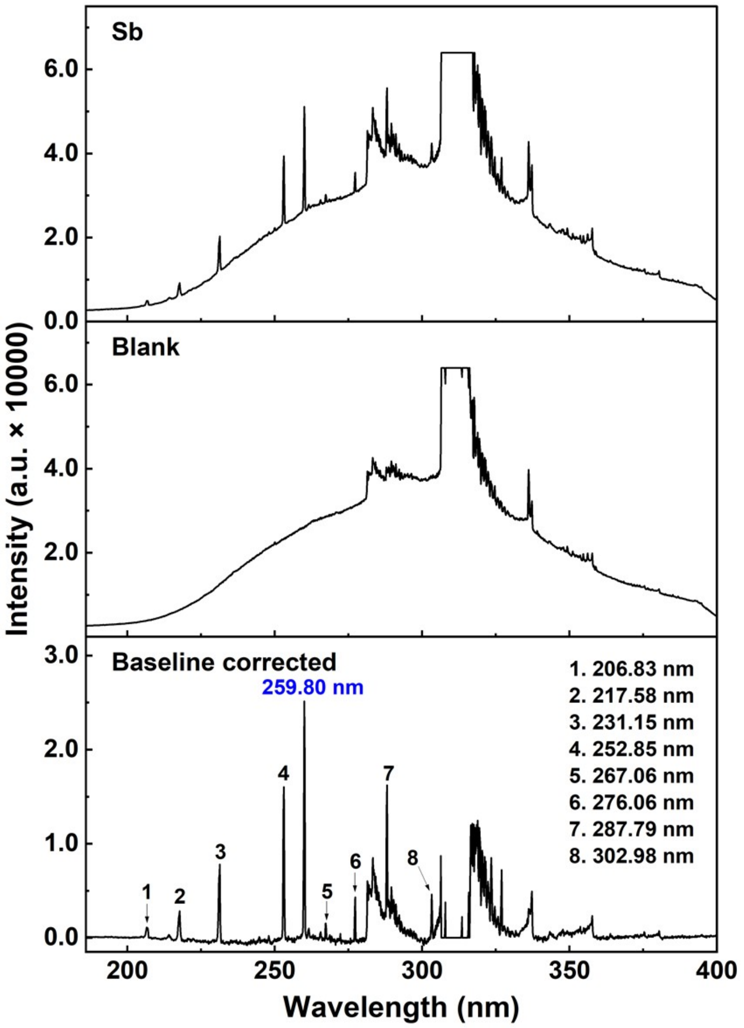

Fig. S3 Characteristic emission spectra of sample (Sb), blank (Ar+H_2), and the spectra after baseline corrected. Experimental details: 0.5 mg L^{-1} Sb; and CCD integration time, 100 ms.

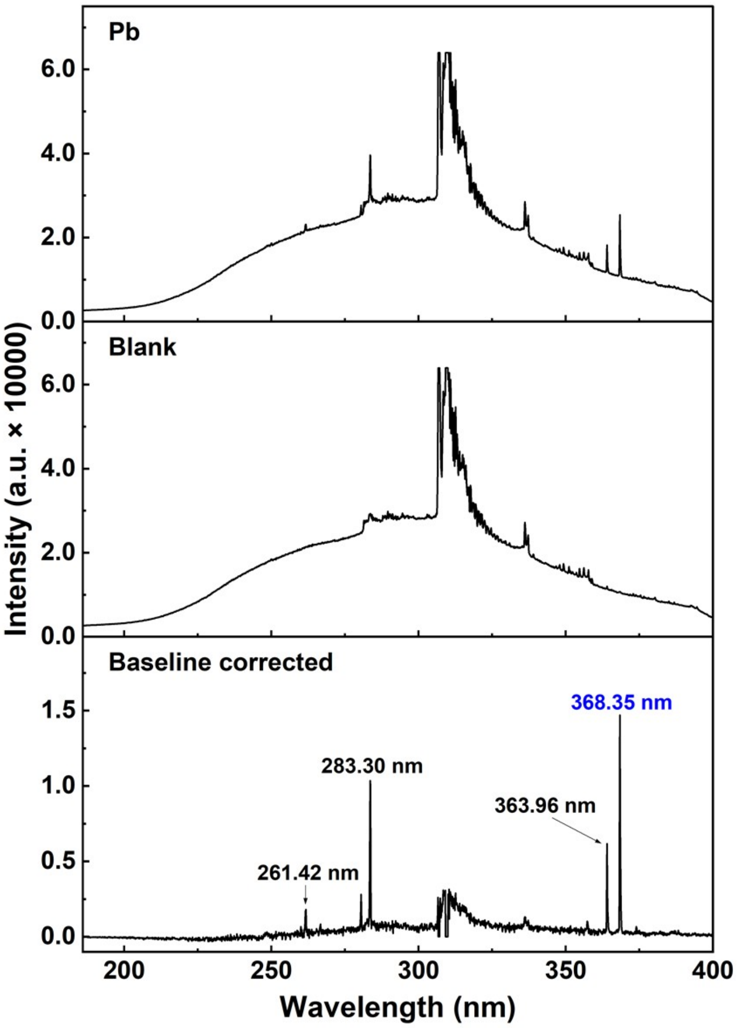

Fig. S4 Characteristic emission spectra of sample (Pb), blank (Ar+H_2), and the spectra after baseline corrected. Experimental details: 0.1 mg L^{-1} Pb; and CCD integration time, 100 ms.

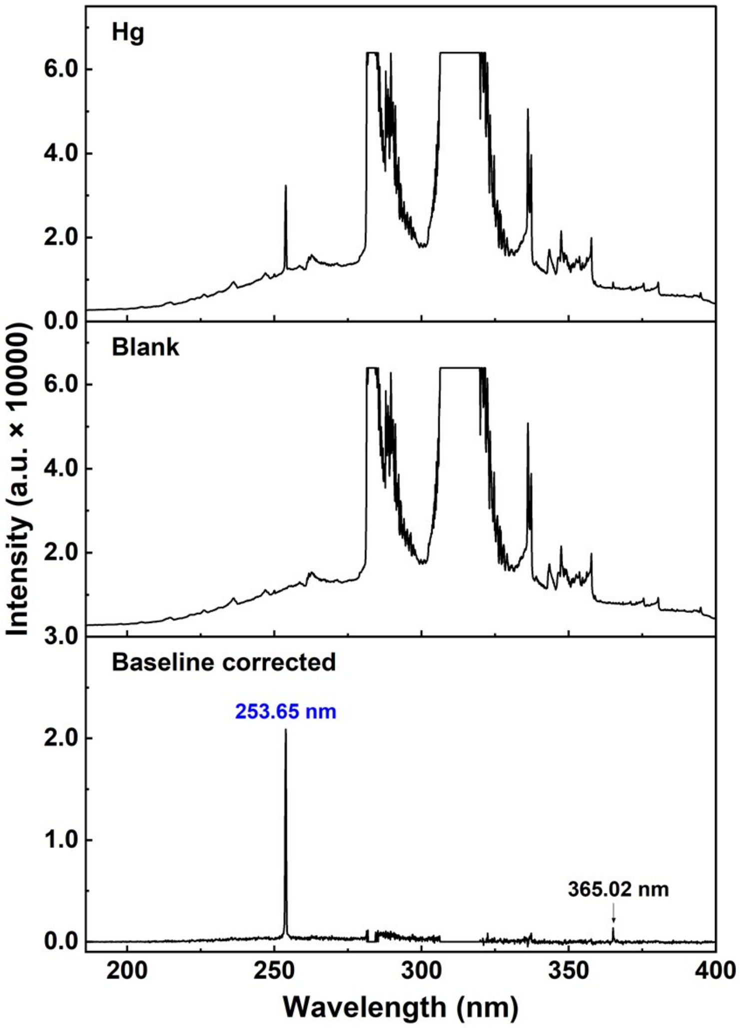

Fig. S5 Characteristic emission spectra of sample (Hg), blank (Ar+H_2), and the spectra after baseline corrected. Experimental details: 0.1 mg L^{-1} Hg; and CCD integration time, 100 ms.

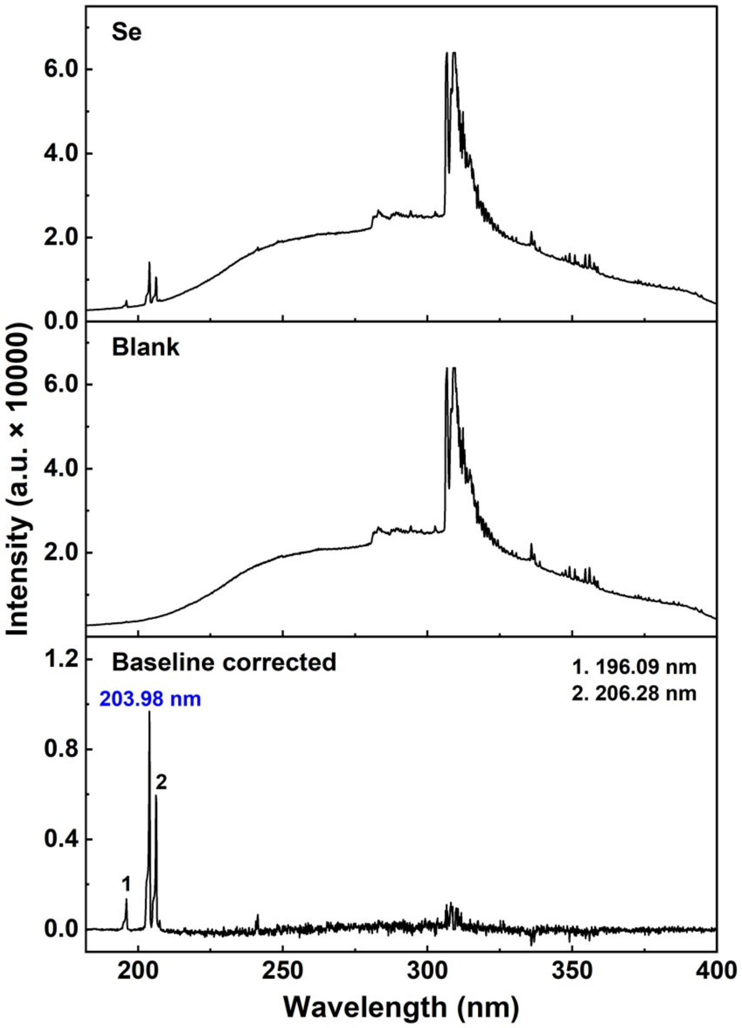

Fig. S6 Characteristic emission spectra of sample (Se), blank (Ar+H_2), and the spectra after baseline corrected. Experimental details: 2.0 mg L^{-1} Se; and CCD integration time, 100 ms.

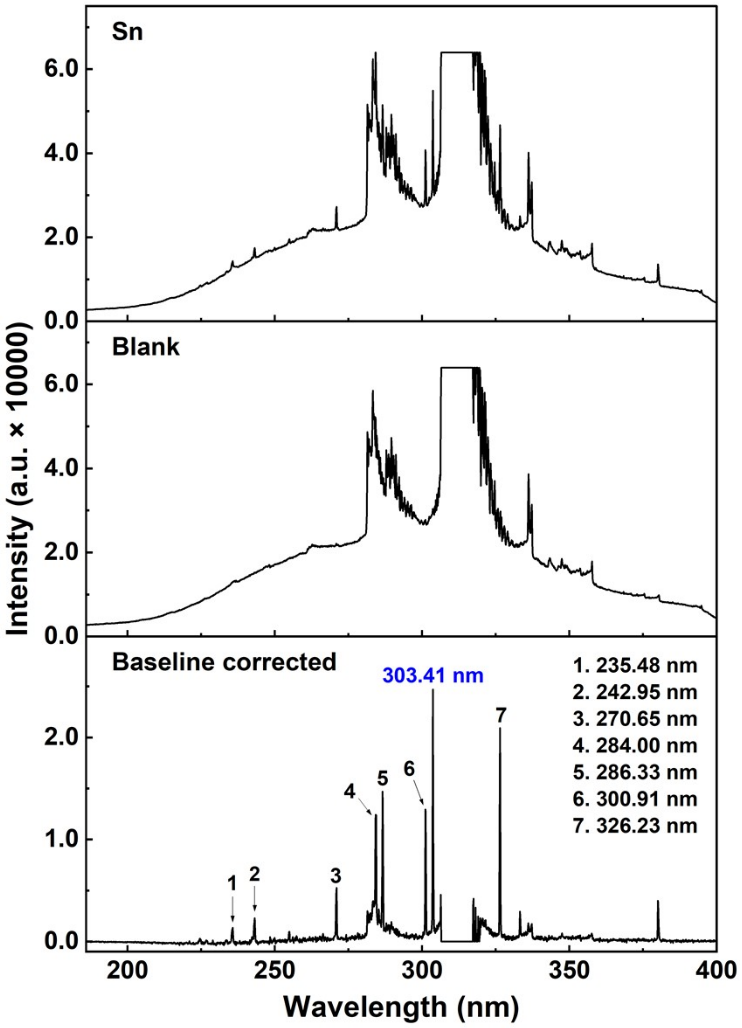

Fig. S7 Characteristic emission spectra of sample (Sn), blank (Ar+H_2), and the spectra after baseline corrected. Experimental details: 0.5 mg L^{-1} Sn; and CCD integration time, 100 ms.

3. Radial confinement effect

Comparison of the two different size radially confined PD-OES devices: both of them were 4 mm in electrode distance, and with a hollow titanium tube electrode (0.9 mm i.d., 1.2 mm o.d.) and a tungsten rod electrode (1 mm diameter). The inner and outer diameters of the small T-shape quartz tube were 1.3 and 2.5 mm, while that of the large one was 2.8 and 5.0 mm, respectively.

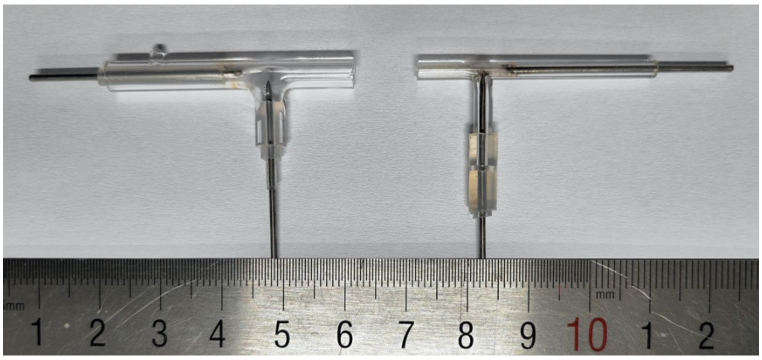

Fig. S8 The photograph of the different size tubes for radially confined PD-OES devices. Left, the larger one; and right, the smaller one.

4. Plasma parameter diagnostics

The emission spectra used for plasma parameter calculations were collected by a Czerny-Turner spectrometer (Andor SR-500i) equipped with an CCD detector (Andor DH340T-18U-E3).

4.1 Rotation temperature (T_{rot})

LIFBASE software was used to simulate the spectral distribution characteristics of the OH radical rotation energy level (306-312 nm, $A^2\Sigma^+, v' = 0 \rightarrow X^2\Pi, v'' = 0$) at different rotation temperatures T_{rot} (K)[1, 2], and then compared with the experimentally measured emission bands, and when the two spectral profiles can be in good overlapping, the T_{rot} corresponding to the simulated spectra is the T_{rot} of the plasma under the experimental conditions. As presented in Fig. S9, the simulated spectrum matches well with the experimental spectrum when the T_{rot} is 1850 K, i.e., the T_{rot} under the experimental conditions is 1850 K. The T_{rot} of the plasma for the other experimental conditions is also obtained by following the similar procedure.

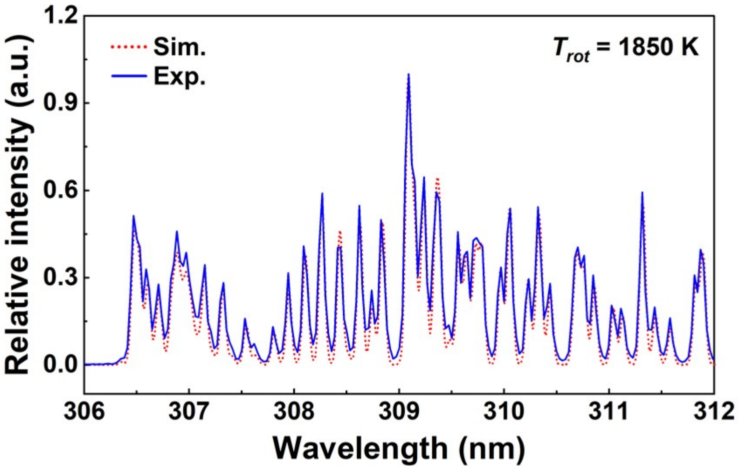

Fig. S9 An example of comparison between the experimental and the simulated spectrum of OH ($A^2\Sigma^+$-$X^2\Pi$, 306-312 nm) for the calculation of rotation temperature.

4.2 Excitation temperature (T_{exc})

The excitation temperature T_{exc} (K) of the microplasma can be calculated by measuring the atomic emission spectral lines and their intensities of Ar residing in different upper energy levels and combining them with the Boltzmann slope method.[3, 4] The relevant calculation formula is as follows:

$$\log \frac{I\lambda}{g_m A_m} = -\frac{0.625}{T_{exc}} E_m + C \tag{S1}$$

where I is the intensity of the emission spectral line, λ is the wavelength of the emission spectral line, g_m is the statistical weight, A_m is the transition probability, E_m is the excitation energy of upper energy levels (cm^{-1}, if the unit is eV, the constant "0.625" needs to be changed to "5040"), and C is a constant.

As can be seen from the formula, the T_{exc} can be calculated by plotting the trend of E_m and Iog($I\lambda/g_m A_m$) according to the emission spectra of Ar atoms in different excited states and performing a linear fit to obtain their slopes (-0.625/T_{exc}). Detailed information about the parameters of the atomic spectral lines of Ar used to calculate the T_{exc} are listed in Table S1, which are referenced from the latest NIST atomic spectra database.[5] Fig. S10 shows an example of the Boltzmann slope method for the calculation of the T_{exc}. All T_{exc} obtained in the experiment are the average of the results of three measurements.

Table S1. Wavelength (λ), excitation energy (E_m), statistical weight (g_m) and transition probability (A_m) of the selected optical emission lines of Ar.[5]

λ (nm)	E_m (cm^{-1})	g_m	A_m (10^7 s^{-1})
800.61	106237	5	0.49
801.48	105617	5	0.93
810.37	106087	3	2.50
811.53	105463	7	3.30
826.45	107496	3	1.53

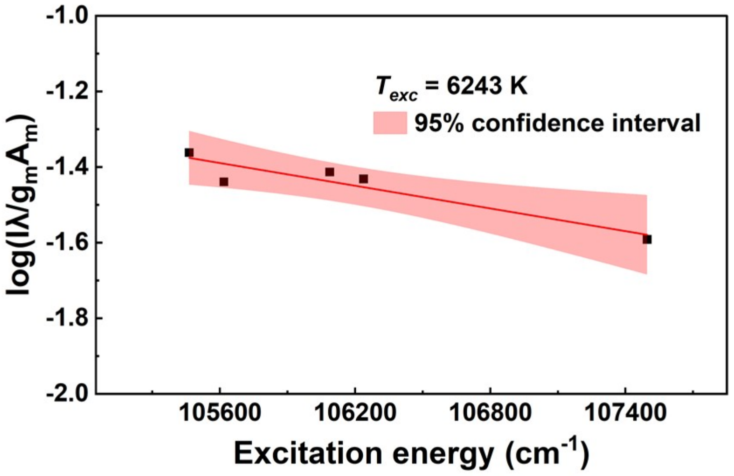

Fig. S10 An example of Boltzmann slope method for the calculation of excitation temperature.

4.3 Electron density (n_e)

In this work, the electron density n_e (cm^{-1}) of the microplasma was calculated from the Stark broadening of the spectral profile of the H$_\beta$ (486.13 nm) emission spectrum,[2, 6] and the main formula is as follows:

$$n_e = 10^{17} \times \left(\frac{\Delta\lambda_s}{4.800} \right)^{1.46808} \tag{S2}$$

where $\Delta\lambda_s$ is the full width at half maximum (FWHM) of the Stark broadening of the H$_\beta$ spectrum, the unit is nm.

The calculation process of the n_e is as follows: firstly, the experimentally measured spectral profile data are normalized, then they are input into MATLAB and compared with the simulated spectral line peak profile obtained by a written procedure and iterate repeatedly to obtain the Stark broadening at the best fit, and then substitute into Eq. (S2) to calculate the n_e at this time. As shown in Fig. S11, it can be seen that the profiles of the simulated spectral lines coincide with the experimentally measured spectral profiles, and the calculated n_e is 5.46 × 10^{14} cm^{-3}.

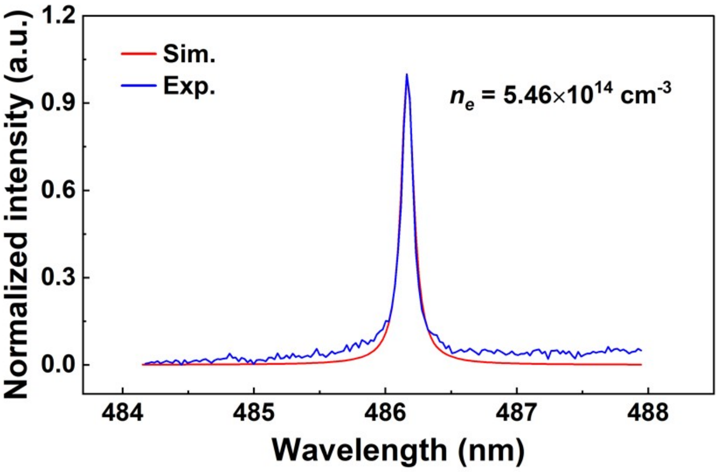

Fig. S11 An example of comparison between the experimental and the simulated H_β (486.13 nm) spectrum for the calculation of electron density.

Table S2. The calculated results of plasma parameters.

Plasma parameter		T_{rot} (K)	T_{exc} (K)	n_e (×10^{14} cm^{-3})
Large size	Ar	1700 ± 50 [a]	4025 ± 238	3.37 ± 0.06
	Ar+H_2	1760 ± 17	5371 ± 203	5.25 ± 0.23
Small size	Ar	1850 ± 30	6224 ± 19	5.29 ± 0.17
	Ar+H_2	1920 ± 26	6834 ± 263	6.31 ± 0.15
Uncertainty [b]		± 2.7%	± 5.9%	± 4.2%

[a] Mean ± standard deviation (n=3); [b] Estimation of measurement uncertainty.

5. Comparison of radial and axial view modes

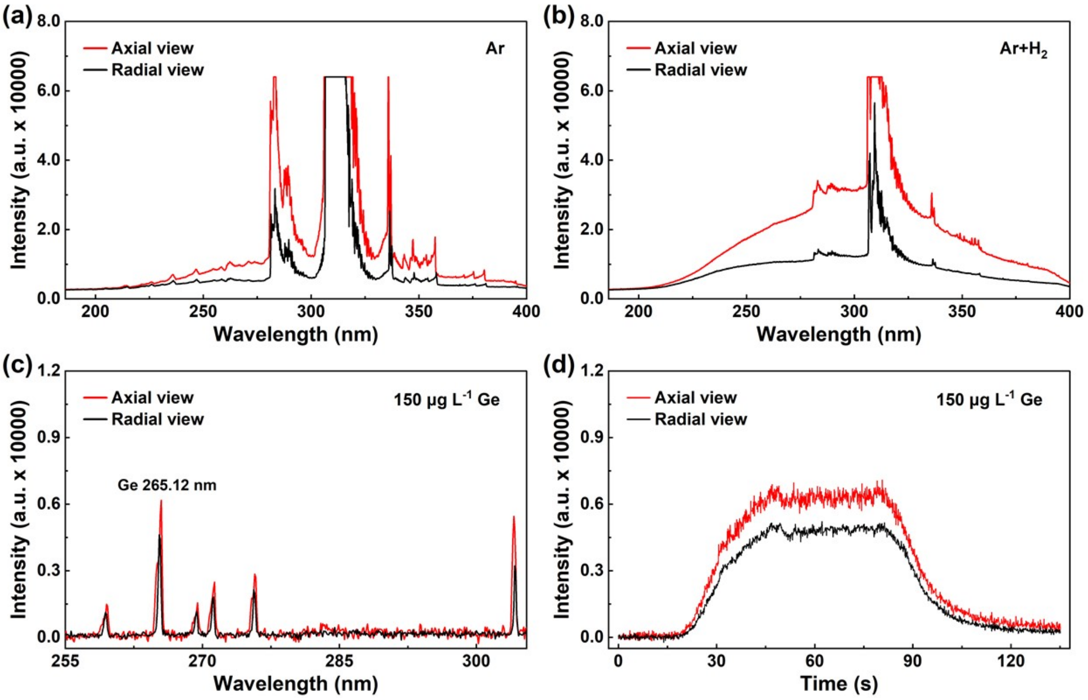

Fig. S12 Comparison of (a) background emission spectra with Ar, (b) blank emission spectra with Ar and H_2, (c) net characteristic emission spectra of Ge, and (d) temporal spectral emission signal of Ge at 265.12 nm from axial view or radial view mode of RC-PD-OES. In the axial view mode, the collimating lens was coaxial with the hollow titanium electrode; and in the radial view mode, the collimating lens was perpendicular to both the hollow titanium electrode and tungsten rod electrode.

6. Selection of experimental conditions

To achieve the best analytical performance of the HG-RC-PD-OES system, the experimental conditions of HG and the instrumental operation parameters of the RC-PD-OES were carefully studied, mainly including the concentration of KBH_4 and HCl, as well as the flow rate of sample and reductant, the flow rate of Ar, and input voltage. The concentrations of 500, 100, 100, 100, 50, 500, and 50 μg L^{-1} for As, Sb, Ge, Pb, Hg, Se, and Sn were used through the optimization experiments, respectively. Before the experiments, 1% (m/v) thiourea and 1% (m/v) ascorbic acid were added to As and Sb solutions for pre-reduction, and 2% (m/v) $K_3[Fe(CN)_6]$ was added to Pb solution for pre-oxidation.[3, 7]

6.1 Experimental conditions of HG

Hydride generation was used as the sample introduction technique to transform the analyte into the volatile species and separate from the sample matrix, and the vapor generation efficiency was related to the HG conditions including the concentration of HCl and KBH_4, as well as the sample flow rate. Consequently, it was essential to study in detail for desired analytical performance.

The concentration of KBH_4 was firstly evaluated over a range from 0.05% to 1.0% (m/v), except a range of 0-0.1% (m/v) for Hg. As revealed in Fig. S13a-b, the signal responses obviously increased and then gradually decreased with KBH_4 concentration, possibly owing to the excess by-product hydrogen diluting the analyte vapor and consuming the energy of the microplasma. Thus, the best KBH_4 concentration of 0.2%, 0.2%, 0.5%, 0.5%, 0.005%, 0.5%, and 0.5% (m/v) was used for the determination of As, Sb, Ge, Pb, Hg, Se, and Sn, respectively. Likewise, considering that high HCl concentration could produce a large amount of hydrogen and moisture, the effect of HCl concentration was then investigated (Fig. S13c-d), and the best signal responses were obtained at 2.0%, 0.5%, 1.0%, 1.0%, 4%, 10%, and 1.0% (v/v) for detection of As, Sb, Ge, Pb, Hg, Se, and Sn, respectively. Due to the reaction time and the amount of analyte transferred to the plasma region per unit time being determined by sample flow rate, the influence of a wide range of flow rate from 1 to 8 mL min^{-1} was further explored, and the result was presented in Fig. S14. The gaseous analytes were more diluted with Ar flow per unit time and the signal trailing was also produced at a low flow rate, whereas the reaction was insufficient between analyte and reductant at a high flow rate. To this end, the most suitable sample flow rate of 3, 4, 2, 6, 6, 5, and 6 mL min^{-1} were utilized for As, Sb, Ge, Pb, Hg, Se, and Sn in subsequent experiments, respectively.

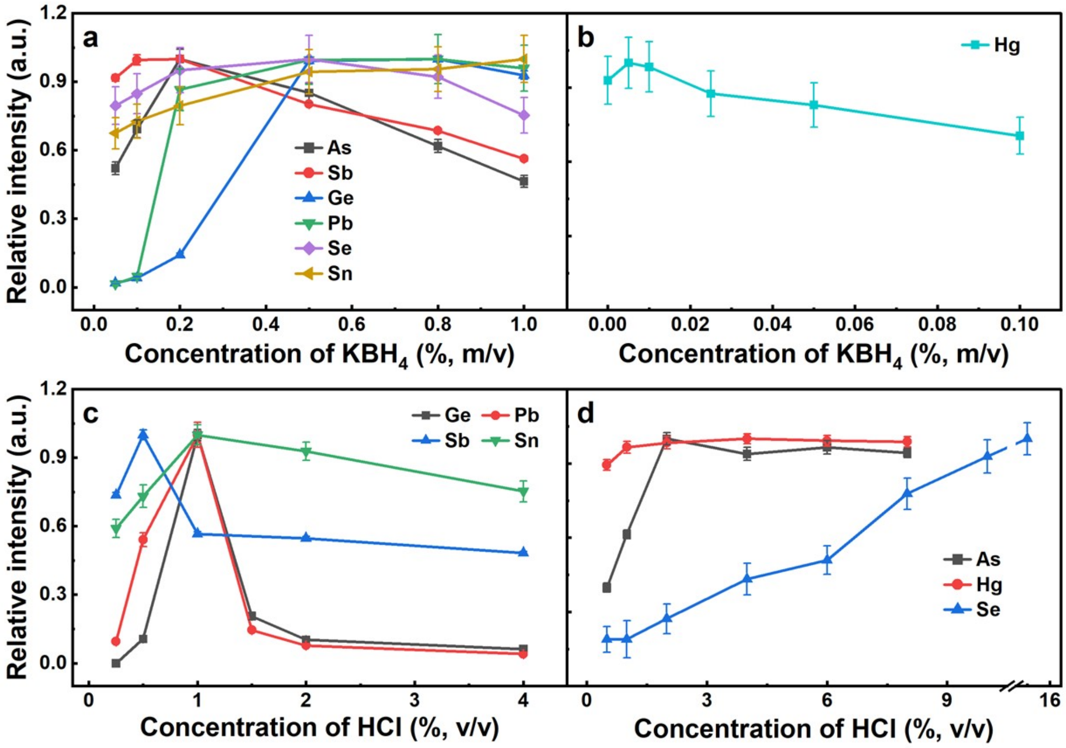

Fig. S13 Effect of (a)-(b) KBH_4 concentration and (c)-(d) HCl concentration. The sample flow rate was 3 mL min^{-1}.

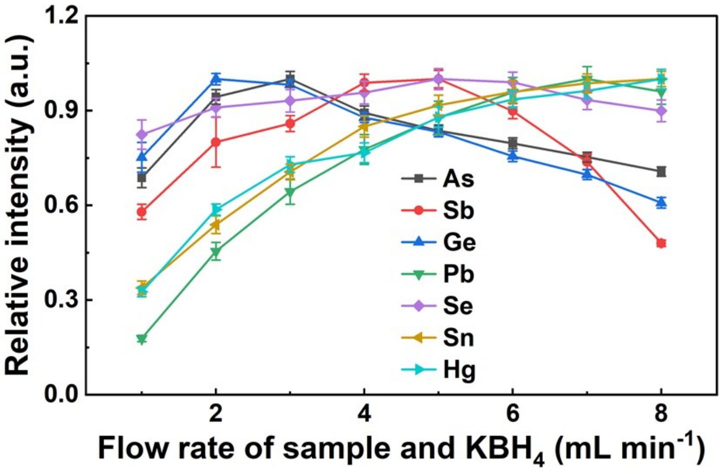

Fig. S14 Effect of flow rate of sample and KBH_4 solutions.

6.2 Flow rate of Ar

The Ar not only serves as discharge gas to maintain the operation of the microplasma but also as the carrier gas to assist sample introduction. The PD microplasma is generated with the breakdown of the discharge gas when it is applied high voltage on two electrodes, and the density of ionized argon affects the excitation capability of the microplasma. Moreover, the carrier gas is used to separate the volatile analyte species from the reaction solution and to purge the analyte vapor into the microplasma region for excitation. Therefore, the flow rate of carrier gas has an important influence on the sample introduction and transport efficiency. As shown in Fig. S15, the effect of Ar flow rate in a range from 50 to 300 mL min^{-1} was explored. If Ar flow rate was too low, it would cause the discharge unstable, poor excitation capability, deterioration of gas-liquid separation effect and transport efficiency. On the contrary, the high flow rate of Ar diluted the analyte vapor, shortened the residence time in the microplasma for excitation, and introduced excess moisture to consume the microplasma energy, resulting in a degraded signal response. In consequence, 200, 150, 150, 150, 50, 200, and 200 mL min^{-1} Ar were chosen as the optimal gas flow rate for the determination of As, Sb, Ge, Pb, Hg, Se, and Sn, respectively.

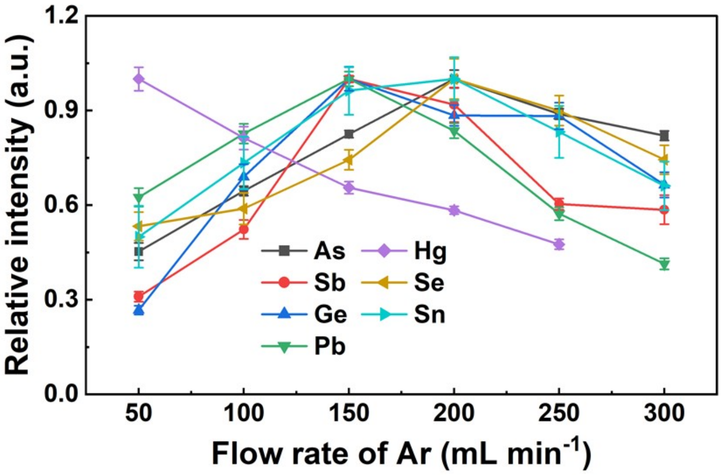

Fig. S15 Effect of flow rate of Ar.

6.3 Input voltage

The excitation capability of the microplasma is dependent on the input voltage. Generally speaking, the higher the input voltage, the stronger the excitation capability. Owing to a neon sign electron transformer was employed to control the discharge voltage, it just needed to adjust its input voltage. Since the input voltage lower than 50 V cannot maintain the normal operation of the microplasma, the range from 60 to 120 V of input voltage was tested (Fig. S16). It was evident that the signal responses increased with the input voltage, while the discharge stability was deteriorated with a too high voltage. Considering both the excitation capability and the stability, an input discharge voltage of 100 V was finally selected for use in subsequent works.

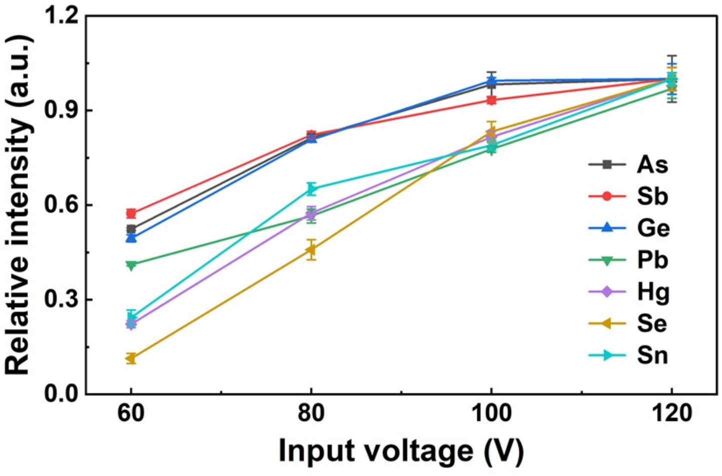

Fig. S16 Effect of input voltage.

Table S3. The selected experimental conditions for each element.

Element	KBH_4 concentration (%, m/v)	HCl concentration (%, v/v)	Flow rate of Ar (mL min^{-1})	Flow rate of sample and KBH_4 (mL min^{-1})
As	0.2	2	200	3
Sb	0.2	0.5	150	4
Ge	0.5	1	150	2
Pb	0.5	1	150	6
Hg	0.005	4	50	6
Se	0.5	10	200	5
Sn	0.5	1	200	6

7. Analytical performance

7.1 Linear calibration curves

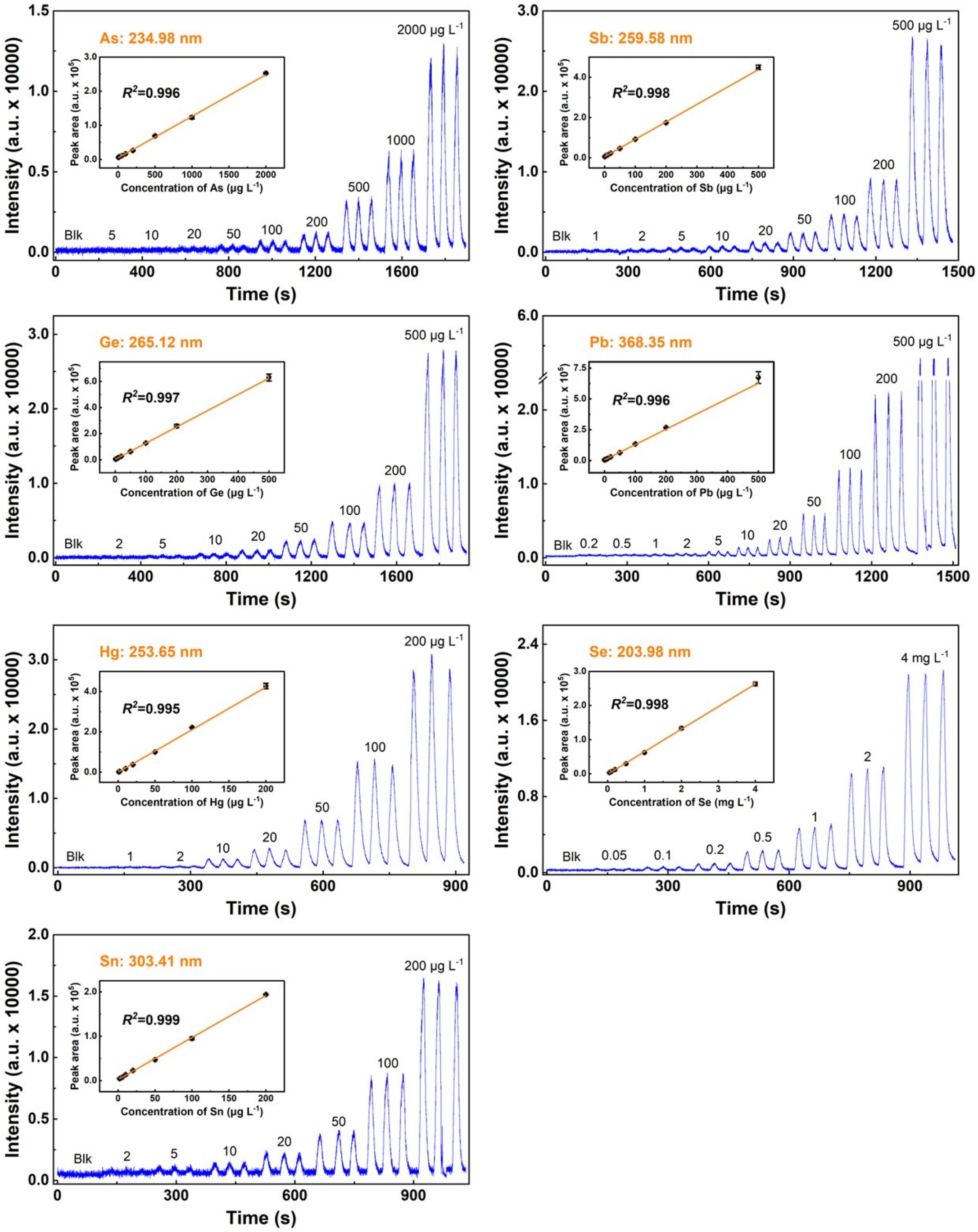

Fig. S17 Temporal spectral emission signal profiles and calibration curves (inset graphs) for analyte elements of As, Sb, Ge, Pb, Hg, Se, and Sn in their linear dynamic ranges. These data were acquired by spectral collection in axial view, and all elements were analyzed separately.

7.2 Relative standard deviation

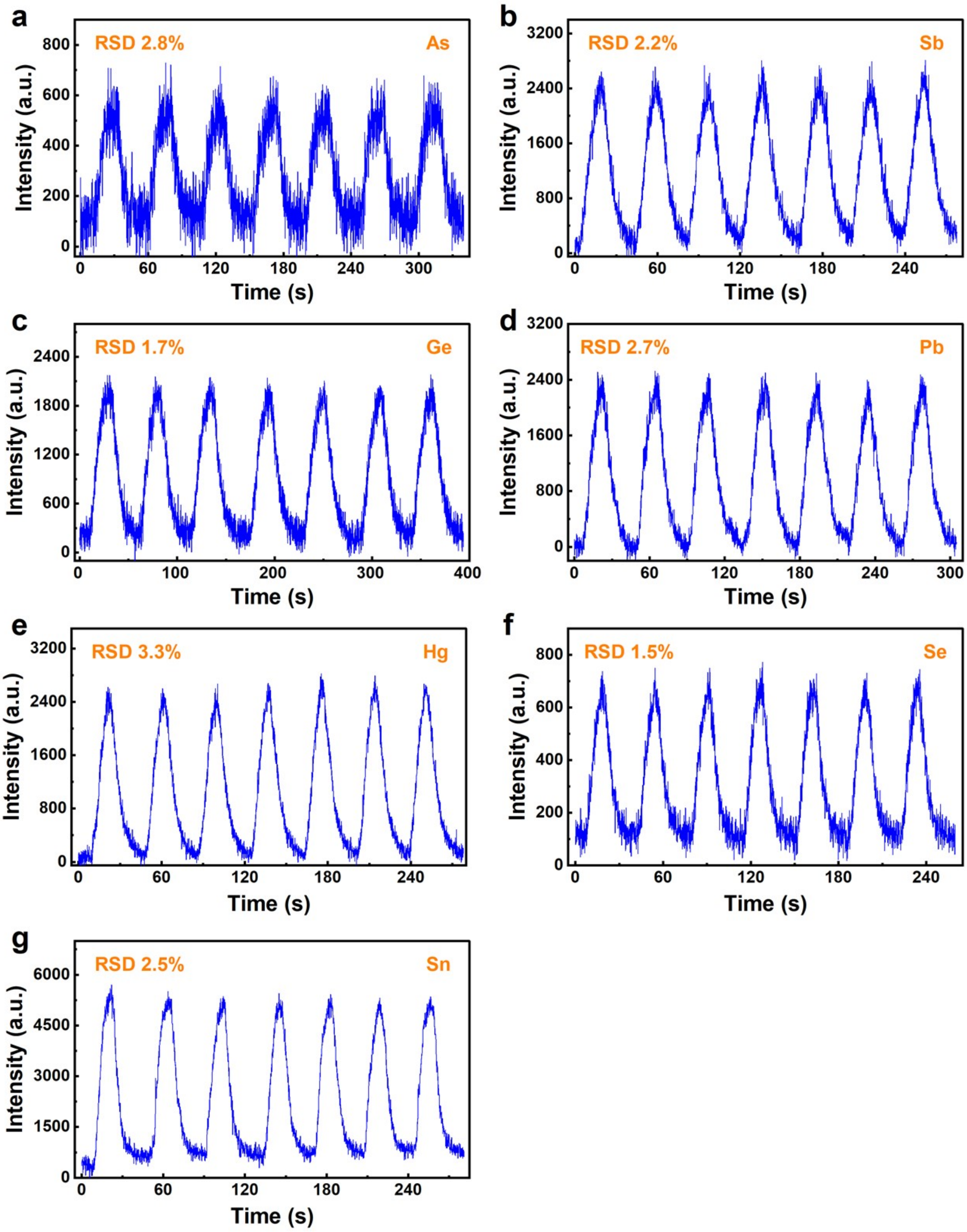

Fig. S18 The relative standard deviations (RSDs) of seven replicate measurements of As, Sb, Ge, Pb, Hg, Se, and Sn at concentrations of 100, 100, 100, and 20, 20, 500, 100 μg L^{-1}, respectively.

7.3 Analytical figures of merit

Table S4. Analytical figures of merit.

Element	LOD (μg L^{-1})	RSD (%)	Linear range (μg L^{-1})	R^2
As	1	2.8	5-2000	0.996
Sb	0.4	2.2	1-500	0.998
Ge	0.5	1.7	2-500	0.997
Pb	0.06	2.7	0.2-500	0.996
Hg	0.09	3.3	1-200	0.995
Se	6	1.5	50-4000	0.998
Sn	0.2	2.5	2-200	0.999

Sample flow rates of As, Sb, Ge, Pb, Hg, Se, and Sn were 3, 4, 2, 6, 6, 5, and 6 mL min^{-1}, respectively; Ar flow rates of As, Sb, Ge, Pb, Hg, Se, and Sn were 200, 150, 150, 150, 50, 200, and 200 mL min^{-1}, respectively; and these were obtained with single element data acquisition mode.

Except for the ICP-OES (with pneumatic nebulization sample introduction), other referenced studies were all based on hydride generation sample introduction. Thanks to the improved excitation capability with the radial confinement effect and the axial view mode to acquire better emission spectral signals, the LODs of As, Sb, Ge, Pb, Hg, Se, and Sn were better or comparable to those by other microplasma-based OES (Table S5).

Table S5. The LODs of this work in comparison with those by other similar methods.

Method	LOD (μg L^{-1})						
	As	Sb	Ge	Pb	Hg	Se	Sn
ICP-OES [8]	1	2	1	1	1	2	2
MIP-OES [9]	1.2	1.8	6.3	-	3.0	3.3	2.4
DBD-OES	4.8 [10]	-	-	8.95 [11]	0.4 [11]	-	-
APGD-OES	4.2 [12]	1.2 [12]	0.5 [13]	0.17 [14]	0.26 [15]	3.1 [12]	0.8 [13]
μCMP-OES [16]	1.4	1.5	-	-	3.0	3.8	-
PD-OES	7 [17]	5 [17]	-	0.73 [18]	-	-	2 [17]
HEPD-OES [3]	2.5	1.5	1.6	2.8	0.10	31	0.24
CrossPD-OES [19]	2.4	-	-	1.9	0.15	-	-
ArrPD-OES [7]	0.7	0.3	0.4	0.7	0.05	2	0.08
RC-PD-OES (This work)	1	0.4	0.5	0.06	0.09	6	0.2

Sample flow rates of As, Sb, Ge, Pb, Hg, Se, and Sn were 3, 4, 2, 6, 6, 5, and 6 mL min^{-1}, respectively; Ar flow rates of As, Sb, Ge, Pb, Hg, Se, and Sn were 200, 150, 150, 150, 50, 200, and 200 mL min^{-1}, respectively; with single element data acquisition mode.

8. Interference study

HG is easily affected by some transition metals,[20, 21] thus the potential interference from several transition metals and some common elements was studied by analyzing 100 μg L^{-1} As, 100 μg L^{-1} Sb, 100 μg L^{-1} Ge, 20 μg L^{-1} Pb, 20 μg L^{-1} Hg, 500 μg L^{-1} Se, and 50 μg L^{-1} Sn, containing Ca^{2+}, Na^{+}, Mg^{2+}, Al^{3+}, Zn^{2+}, Fe^{3+}, Co^{2+}, Ni^{2+}, and Cu^{2+}. As presented in Fig. S19a, these coexisting ions had no significant influence on the determination of As, Sb, Pb, and Hg, whereas 10 mg L^{-1} Zn^{2+}, Co^{2+}, and Cu^{2+} had obvious interference with the detection of Ge, resulting the recoveries down to 43%, 57%, and 72%, respectively; 10 mg L^{-1} Fe^{3+}, Co^{2+}, Ni^{2+}, and Cu^{2+} had remarkable negative interference with the detection of Sn, with the recoveries of 79%, 48%, 14%, 43%, respectively; and 10 mg L^{-1} Cu^{2+} had obvious negative interference with the detection of Se, with the recovery of only 26%. Fortunately, further investigation found that the inhibition effect of Zn^{2+} could be eliminated with 100 mg L^{-1} EDTA, and the interferences from Fe^{3+}, Co^{2+}, Ni^{2+}, and Cu^{2+} were successfully suppressed with 200 mg L^{-1} DDTC (Fig. S19b). However, the interference of Cu^{2+} with the determination of Se could not be masked by EDTA and DDTC, possibly owing to the hyperacidity of the sample solution (10% (v/v) HCl). After further attempting several masking agents including thiourea, sodium thiosulfate ($Na_2S_2O_3$), and $K_3[Fe(CN)_6]$, it was found that 2% (m/v) $K_3[Fe(CN)_6]$ successfully removed the negative effect from Cu^{2+}. Additionally, these coexisting elements were generally of low concentrations in most samples such as natural water samples, and it could also be addressed with sample pretreatment such as simple dilution or the addition of matrix masking reagents.

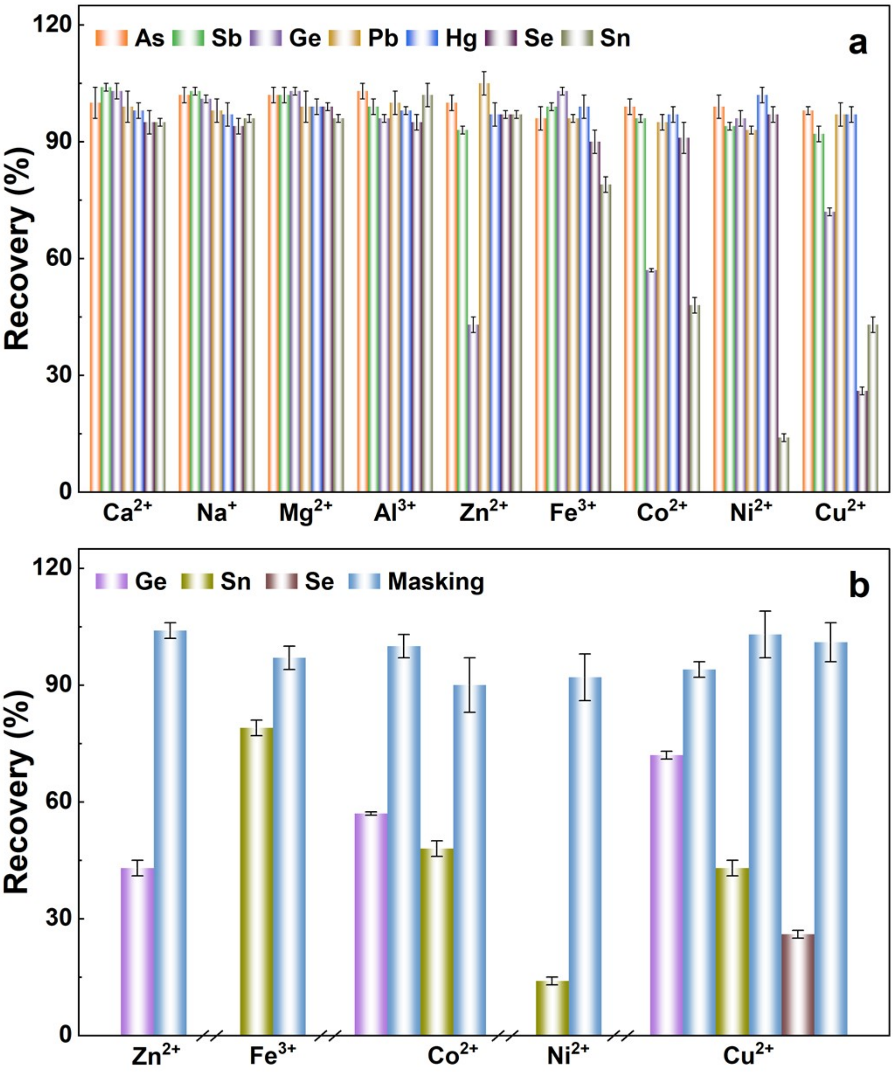

Fig. S19 Influence of (a) 100 mg L^{-1} Ca^{2+}, Na^{+}, Mg^{2+}, Al^{3+}, and Zn^{2+}, and 10 mg L^{-1} Fe^{3+}, Co^{2+}, Ni^{2+}, and Cu^{2+} on the determination of As, Sb, Ge, Pb, Hg, Se, and Sn, respectively; (b) the interference elimination for Ge, Sn, and Se.

9. References

1. P. Bruggeman, E. Ribežl, A. Maslani, J. Degroote, A. Malesevic, R. Rego, J. Vierendeels and C. Leys, *Plasma Sources Science and Technology*, 2008, **17**, 025012.
2. H. Yuan, J. Feng, D. Z. Yang, X. F. Zhou, J. P. Liang, L. Zhang, Z. L. Zhao and W. C. Wang, *Journal of Applied Physics*, 2020, **128**, 093303.
3. M. T. Li, K. Li, L. He, X. L. Zeng, X. Wu, X. D. Hou and X. M. Jiang, *Anal. Chem.*, 2019, **91**, 7001-7006.
4. Y. Cai, Y. L. Yu and J. H. Wang, *Anal. Chem.*, 2018, **90**, 10607-10613.
5. NIST Atomic Spectra Database., National Institute of Standards and Technology, https://physics.nist.gov/PhysRefData/ASD/lines_form.html.
6. H. Yuan, D. Z. Yang, X. Li, L. Zhang, X. F. Zhou, W. C. Wang and Y. Xu, *Physics of Plasmas*, 2019, **26**, 053505.
7. M. Zhang, Q. S. Tang, P. X. Li, L. He, X. D. Hou and X. M. Jiang, *Anal. Chem.*, 2023, **95**, 5151-5158.
8. PerkinElmer Inc., *Atomic spectroscopy: A guide to selecting the appropriate technique and system*, PerkinElmer Inc.: Waltham, MA, U.S.A., 2008, p 14.
9. H. Matusiewicz and M. Ślachciński, *Microchem. J.*, 2010, **95**, 213-221.
10. Z. L. Zhu, H. Y. He, D. He, H. T. Zheng, C. X. Zhang and S. H. Hu, *Talanta*, 2014, **122**, 234-239.
11. N. Li, Z. C. Wu, Y. Y. Wang, J. Zhang, X. N. Zhang, H. N. Zhang, W. H. Wu, J. Gao and J. Jiang, *Anal. Chem.*, 2017, **89**, 2205-2210.
12. K. Greda, P. Jamroz, D. Jedryczko and P. Pohl, *Talanta*, 2015, **137**, 11-17.
13. C. C. Huang, Q. Li, J. M. Mo and Z. Wang, *Anal. Chem.*, 2016, **88**, 11559-11567.
14. J. Q. Cheng, Q. Li, M. Y. Zhao and Z. Wang, *Anal. Chim. Acta.*, 2019, **1077**, 107-115.
15. R. Rong, Z. Q. Cai, X. Y. Li and Z. Wang, *J. Anal. At. Spectrom.*, 2022, **37**, 2377-2382.
16. H. Matusiewicz and M. Ślachciński, *Spectrochim. Acta, Part B*, 2017, **133**, 52-59.
17. M. T. Li, Y. J. Deng, C. B. Zheng, X. M. Jiang and X. D. Hou, *J. Anal. At. Spectrom.*, 2016, **31**, 2427-2433.
18. L. B. He, Y. Lin, P. P. Chen, Y. B. Su, Y. Y. Li and C. B. Zheng, *J. Hazard. Mater.*, 2022, **439**, 129607.
19. L. He, P. X. Li, K. Li, T. Lin, J. Luo, X. D. Hou and X. M. Jiang, *J. Anal. At. Spectrom.*, 2021, **36**, 1193-1200.
20. R. C. de Campos, P. Grinberg, I. Takase and A. S. Luna, *Spectrochim. Acta, Part B*, 2002, **57**, 463-472.
21. W. Zou, C. H. Li, J. Hu and X. D. Hou, *Talanta*, 2020, **218**, 121128.